

Design of a Small Animal PET Imaging System With 1 Microliter Volume Resolution

Ned C. Rouze, *Member, IEEE*, Matthias Schmand, *Member, IEEE*, Stefan Siegel, *Member, IEEE*, and Gary D. Hutchins

Abstract—The design of a new scanner for use in small animal PET imaging is described. The goal is to achieve 1 mm FWHM resolution in each of three orthogonal directions throughout a volume suitable for whole body mouse imaging, roughly 40 mm diameter \times 80 mm long. Simultaneously, the design should achieve a sensitivity of greater than 5% of all decays from a point source located at the center of the scanner.

The scanner uses 12, plane detector banks mounted in a 160 mm diameter ring on a rotating gantry. Each detector bank consists of a 48×108 array of 20 mm long LSO crystals with an array pitch of 0.87 mm. Each bank uses two Hamamatsu H8500 large-area, multi-anode photomultiplier tubes for fluorescence detection. The detector banks are divided into two sets with the respective lines of response offset by one quarter of the array pitch to give increased sampling density.

Tests using a prototype crystal array demonstrate that individual crystals can be resolved. Simulations have been performed to evaluate the performance expected in the complete scanner. With F-18 point sources, the FWHM resolutions in the radial, tangential, and axial directions are less than 1 mm for source positions throughout the desired field of view (FOV). Simultaneously, the detector sensitivity is greater than 7% of all decays for a point source located at the center of the FOV. Results are also presented for simulations using different PET isotopes to investigate the effect of positron range, and for a phantom containing hot spots added to a uniform background to evaluate the scanner performance for an extended object.

Index Terms—Positron emission tomography (PET), positron emission tomography (PET) instrumentation, small animal imaging.

I. INTRODUCTION

MOLECULAR imaging in small animals offers tremendous potential as a tool in many areas including drug development, monitoring gene expression and therapy, and the development of animal models of disease. In particular, positron emission tomography (PET) allows quantitative measurement of the distribution of radiolabeled tracers and the temporal variation of this distribution in response to physiological processes.

Manuscript received November 15, 2003; revised March 3, 2004. This work was supported in part by NIH/NCI Grant P20 CA86350, in part by a Grant from the State of Indiana 21st Century Research and Technology Fund "Indiana Center of Excellence in Biomedical Imaging," and in part by the Indiana Genomics Initiative. The Indiana Genomics Initiative is supported in part by the Lilly Endowment.

N. C. Rouze and G. D. Hutchins are with the Department of Radiology, Division of Imaging Science, Indiana University School of Medicine, Indianapolis, IN 46202 USA (e-mail: nrouze@iupui.edu; gdhutchi@iupui.edu).

M. Schmand is with CPS Innovations, Inc., Knoxville TN 37932 USA (e-mail: Matthias.Schmand@cspet.com).

S. Siegel is with Concorde Microsystems, Inc., Knoxville, TN 37932 USA (e-mail: ssiegel@cms-asic.com).

Digital Object Identifier 10.1109/TNS.2004.829738

These measurements are noninvasive, and thereby allow the response to therapy to be studied longitudinally within the same animal during a course of treatment.

Recently, several PET scanners designed for use in small animal imaging applications have been described [1]–[17]. Although the performance of these scanners varies widely, they typically give a resolution on the order of 1.0–2.5 mm FWHM and a sensitivity of less than 3% of all decays for a point source positioned at the center of the field-of-view (FOV).

This report describes the design of a new PET scanner for use in small animal imaging studies. Our goal is to achieve 1 mm FWHM resolution in the radial, tangential, and axial directions throughout a FOV suitable for whole body mouse imaging, roughly 40 mm diameter \times 80 mm long. Simultaneously, the scanner should have a sensitivity of 5% (or greater) for decay events from a point source located at the center of the scanner.

The design of the new scanner has been developed based on our experience with the IndyPET [1] and IndyPET-II [2] scanners. The distinguishing feature of these scanners is the use of plane detector banks mounted on a rotating gantry. By observing coincidence events between opposing detector banks, parallax is minimized so that thinner crystals can be used to achieve high resolution, and at the same time, longer crystals can be used to achieve high sensitivity. Also, this configuration gives approximately uniform resolution across the FOV. Event data are collected in list mode format, and masking can be applied retrospectively to remove events from lines of response that are particularly sensitive to parallax, thereby giving a tradeoff between resolution and sensitivity. Gantry rotation allows the entire sinogram space to be sampled. In addition, gantry rotation allows pairs of detector banks to be offset to give interspersed lines of response and increased sampling density. This procedure is similar to the effect of detector wobble that has been implemented on some complete ring scanners and has been used successfully with the IndyPET-II [2] scanner to enhance the FWHM resolution by roughly 20% compared to measurements performed without using interspersed lines of response.

The remainder of this report is arranged as follows. Section II describes the design of the new scanner, including the design of the detector banks and the layout of the complete scanner. Also, the results from two preliminary tests of the crystals and PMTs used in the detector banks are presented to demonstrate the ability to resolve individual crystal segments in the detector banks. Section III describes simulations that have been performed to evaluate the performance of the new scanner. A series of simulations using F-18 point sources was used to evaluate the resolution and sensitivity as a function of source position rela-

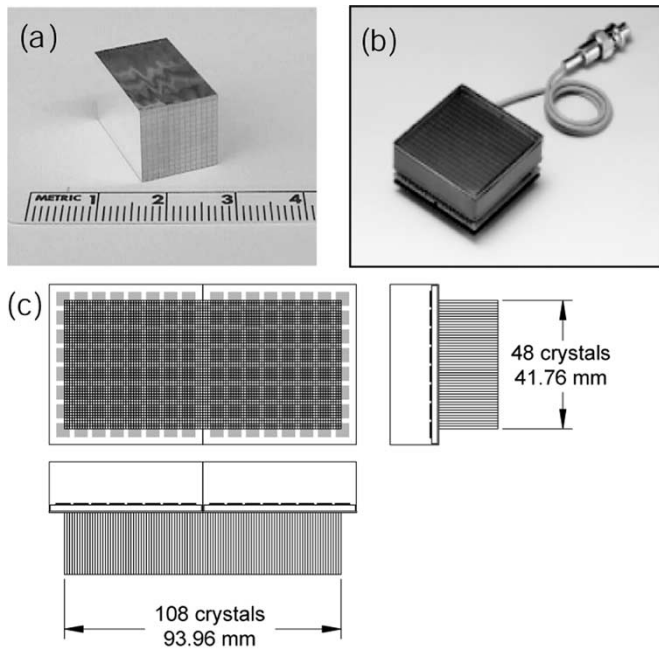


Fig. 1. (a) Sample 14×14 crystal array consisting of 20 mm long LSO crystals with an array pitch of 0.87 mm. (b) Hamamatsu H8500 large-area multianode PMT. (c) The complete detector banks will use two H8500 PMTs to detect light from a 48×108 crystal array. Gray squares on the sketch represent the effective anode regions in the PMTs.

tive to the center of the scanner. Simulations using point sources have also been performed using different PET isotopes to evaluate the effect of positron range. In addition, a simulation using hot spots added to a uniform background has been performed to evaluate the scanner performance for extended objects. Finally, Section IV gives some discussion and concluding remarks.

II. SCANNER DESIGN

A. Detector Banks

The detector banks in the new scanner will take advantage of two components that have recently become available. First, the scintillation crystals will consist of LSO crystal arrays manufactured by Concorde Microsystems, Inc. Fig. 1(a) shows a prototype 14×14 array that has been used in preliminary tests described below. The array consists of 20 mm long crystals with an array pitch of 0.87 mm joined with a dielectric reflector material between the crystals. The thickness of the reflector and adhesive is approximately 0.07 mm so that the dead space introduced by the reflector reduces the active area of the array to 84% of the physical area. Second, fluorescence from the crystals will be detected by Hamamatsu H8500 PMTs, one of which is pictured in Fig. 1(b). These PMTs are 52 mm square and have an active area of 49 mm square. Signal readout is performed using an 8×8 grid of anodes with a spacing of 6.08 mm. A complete detector bank is sketched in Fig. 1(c). Each detector will use a 48×108 crystal array with overall dimensions of 41.76 mm \times 93.96 mm. Fluorescence from the array is detected by two Hamamatsu H8500 PMTs.

Two preliminary tests have been performed to evaluate the combination of crystal arrays and PMTs. First, to determine if individual crystal segments can be resolved, the test array shown

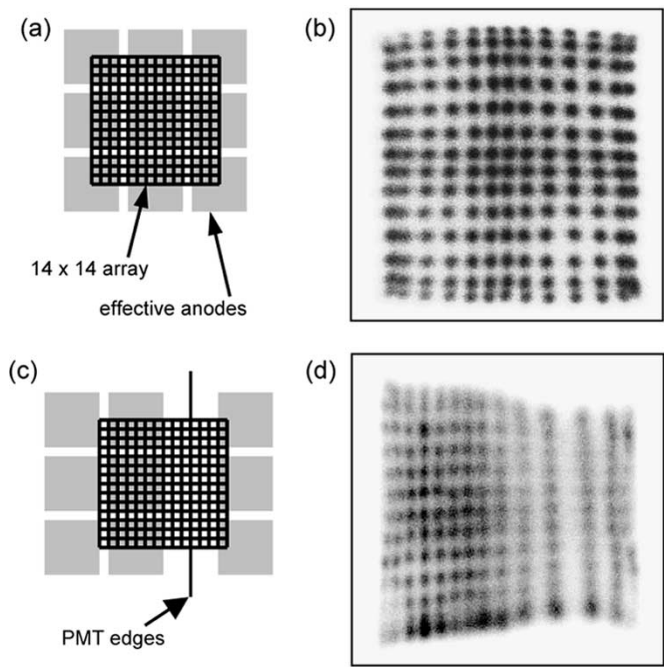


Fig. 2. Preliminary tests used to investigate the ability to resolve individual crystal segments. (a) In the first test, the crystal array shown in Fig. 1(a) was positioned over nine anodes in one H8500 PMT, and the anode signals were weighted according to their X and Y positions to give the position profile shown in (b). In the second test, the test array was positioned over the gap between two adjacent PMTs as shown in (c). The profile shown in (d) indicates that crystals can be resolved across the gap between PMTs, and that compensation for variable anode gains will be required.

in Fig. 1(a) was positioned over a 3×3 anode region of one H8500 PMT as shown in Fig. 2(a). Signals from the nine anodes were digitized and summed by weighting each signal according to its X and Y position. The resulting profile shown in Fig. 2(b) demonstrates that individual crystal segments can be resolved.

The second test investigated the possibility of resolving crystal segments across the gap between two PMTs. This is possible because the front window of the H8500 PMT is attached to the PMT case so that light can enter the PMT through the edge of the window. For this test, a 0.5 mm thick glass plate was positioned over two PMTs, and optical grease was placed in the gap between the edges of the windows to increase the light transmission through the edges. The test crystal was positioned over a nine anode region divided between the two PMTs as shown in Fig. 2(c). The measured profile is shown in Fig. 2(d) and indicates that each of the 14 columns in the array can be identified. The narrowing of the measured profile across the gap between PMTs is caused by the different anode gains in the two tubes and indicates that it will be necessary to compensate for the variable gains of the individual anode signals.

B. Scanner Layout

As shown in Fig. 3, the new scanner will use 12 detector banks mounted in a 160 mm diameter ring. To minimize parallax caused by photon penetration in the crystals, one option is to consider only events between opposing detector banks. In this case, the FOV has a 41.7 mm diameter as indicated by the inner dashed circle in Fig. 3. It is also possible to enlarge the FOV by

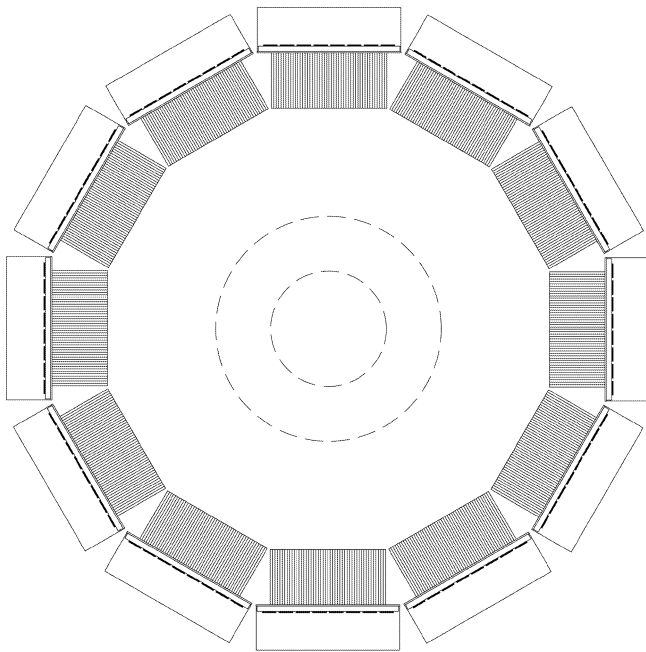


Fig. 3. Layout of the complete scanner. Twelve detectors are arranged in a 160 mm diameter ring. For coincidence events between opposing detector banks, the FOV is 41.7 mm (inner dashed circle). For coincidence events between each detector bank and the opposing and adjacent (tilted) banks, the FOV is 81.7 mm (outer dashed circle).

including events between each detector bank and the opposing and adjacent tilted banks. In this case, the FOV has an 81.7 mm diameter as indicated by the outer dashed circle in Fig. 3.

The detector banks will be mounted on a rotatable gantry, and data will be acquired during continuous gantry rotation. To increase the sampling density, the six pairs of opposing detector banks will be divided into two sets, and the detector banks in one set will be offset relative to the other by one quarter of the crystal array pitch (0.2175 mm). Fig. 4 illustrates this effect. After collecting data with a full range of gantry positions and rebinning the events into parallel lines of response for each sinogram angle, the projection spacing is one quarter of the array pitch. This procedure has been used successfully with the IndyPET-II [2] scanner to give increased resolution of roughly 20% compared to measurements performed without the interspersed lines of response. Simulations presented in Section III indicate that a similar increase in resolution will be realized in the new scanner.

III. SIMULATIONS

The University of Washington package SimSET [18] has been used to perform simulations to predict the performance of the new scanner. Simulations using F-18 point sources were used to investigate the scanner resolution and sensitivity as a function of source position. The effect of positron range was also investigated using point source simulations with different PET isotopes. In addition, a simulation using hot spots added to a uniform background has been performed to evaluate the scanner performance for extended objects.

For the scanner configuration shown in Fig. 3, simulations were performed for coincidence events between opposing de-

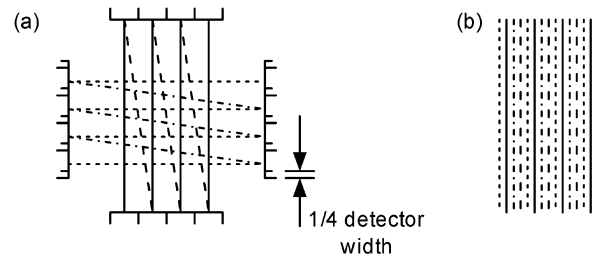


Fig. 4. Illustration showing the increased sampling density possible using detector banks offset by one quarter of the crystal array pitch. For clarity, only two pairs of detector banks are shown. (a) Example lines of response collected at a specific gantry position. (b) Illustration of the lines of response for one sinogram angle after collecting data over a complete range of gantry positions and rebinning the data. After rebinning, the projection spacing is one quarter of the array pitch.

tor banks and between each detector bank and the tilted banks adjacent to the opposing bank. The opposing detector banks were modeled using the SimSET “dual-headed coincidence” mode. The tilted detector banks were modeled by modifying the SimSET code to account for changes in the angle of incidence of photons onto the detector. Gantry rotation was modeled by selecting the gantry angle from one of 1200 positions in 180°.

The simulations included the effect of positron range, photon noncollinearity, and photon scatter in the source and detectors. No attempt was made to account for the position or attenuation coefficient of the intracrystal reflector when tracking photons through the crystal array. However, the dead space introduced by the reflector was included when estimating the detection sensitivity (see below). Photon events in each detector were identified using a 350–650 keV energy window. For each coincidence event, the photon positions in the detector banks were recorded in a list mode event file. Events were binned into crystal segments retrospectively to allow the same data set to be used for cases with detector banks positioned normally and with the detector banks offset by one-quarter of the array pitch. Results obtained by including, and excluding, this bank offset option in the sorting and reconstruction procedures are included with each of the simulations described below.

Coincidence events were sorted into sinograms using Fourier rebinning [19]. The range of oblique planes was limited to an axial position difference with $\Delta z \leq 48$ crystals to reduce the effects of parallax and enhance the axial resolution. Similarly, some lines of response were excluded in the sorting process to limit the effects of parallax from the tilted detector banks near the center of the FOV. This masking was performed using the transaxial mask shown in Fig. 5. All of the events detected between opposing detector banks were included. For events between each detector bank and the tilted banks adjacent to the opposing bank, only the events in the hatched portion of the sinogram range indicated in Fig. 5 were included.

Using Fourier rebinning, it is possible to obtain sinogram planes at any axial position, not just at the position of direct and cross planes. This has been used to increase the density of axial planes in a manner analogous to the use of offset detector banks to increase the projection density in an axial plane. Results obtained by including, and excluding, this midplanes option in the sorting and reconstruction procedures are included for each of the simulations presented below.

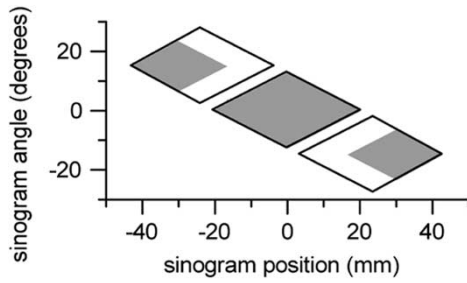


Fig. 5. Event mask applied when sorting coincidence events into sinograms. For opposing detector banks (center diamond), all events are included. For events between each detector bank and the tilted banks adjacent to the opposing bank, only events in the hatched areas are included to reduce the effects of parallax near the center of the FOV.

A. Resolution and Sensitivity

The resolution and sensitivity of the scanner were evaluated using a series of simulations with F-18 point sources positioned at radial positions of 0, 5, 10, \dots , 40 mm from the center of the scanner. The source was embedded in a 5 mm diameter water sphere to provide sites for positron annihilation. (This size was chosen empirically to optimize the tradeoff between an increase in the number of annihilation events, and increased attenuation, with larger spheres.) A total of 10^9 decays were simulated for each source. Images were reconstructed using filtered backprojection with a ramp filter.

Fig. 6 shows sample sinograms and reconstructed images for point sources located at positions of 15 mm and 35 mm from the center of the FOV. For the 15 mm position, the mask in Fig. 5 removes most of the lines of response from the tilted detector banks, giving a narrow sinogram trace and an approximately symmetric image. For the source at a position of 35 mm, the parallax introduced by the tilted detector banks results in a sinogram trace that is broadened in those areas where there are contributions from the tilted detector banks, and the resulting image is elongated in the radial direction.

Fig. 7 shows resolution and sensitivity results as a function of source position. The FWHM and FWTM widths in the radial, tangential, and axial directions were determined from profiles through the center of the reconstructed image. The FWHM volume resolution was calculated as the product of the FWHM resolution values in the three orthogonal directions. The sensitivity results were determined as the ratio of the number of coincidence events (after masking) compared to the number of simulated decays. A correction factor of 0.71, obtained from the dead space factor of 0.84 (see Section II-A) for each of two detectors, was included in the sensitivity calculation to compensate for the dead space introduced by the reflector in the crystal arrays.

Two results are presented for each quantity plotted in Fig. 7. The closed symbols show results obtained by including the offset detector banks and midplanes options in the sorting and reconstruction procedures. The open symbols give results with these options omitted. We observe that the inclusion of the bank offset and midplanes options enhances the resolution for each of the three directions by a factor of roughly 20%, and that the volume resolution is enhanced significantly. In addition, results for the volume resolution are shown for the cases in which

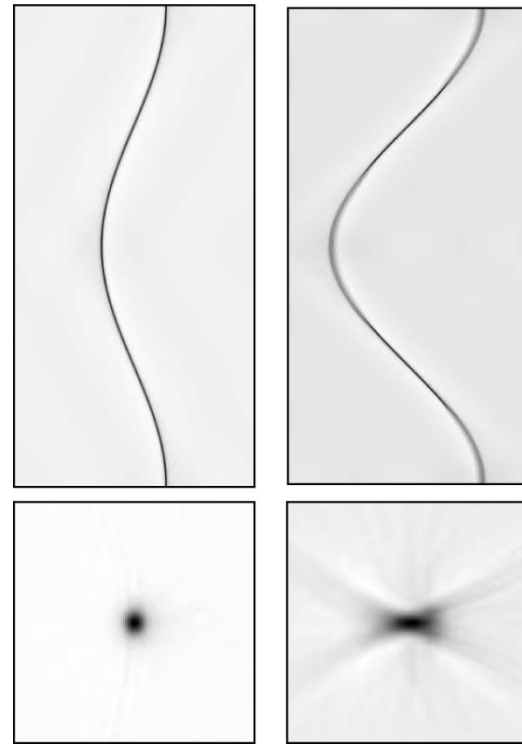


Fig. 6. Sample sinograms (top) and reconstructed images (bottom) for point sources located at positions of 15 mm (left) and 35 mm (right) from the center of the scanner FOV. The images are 10 mm square, and the width of each sinogram is approximately 110 mm.

only the bank offset (dotted line) or midplanes (dashed line) options are included. For these cases, the results in the radial, tangential, and axial directions are nearly identical to one of the two curves obtained with both options either included or excluded, and these plots are not shown for the sake of clarity. The results are as expected; when only the bank offset option is included, the radial and tangential resolution are improved and the axial resolution is not significantly affected, and when only the midplanes option is included, the axial resolution is improved and the radial and tangential resolution are not significantly affected. The total number of coincidence events, and, hence, the sensitivity, is the same for each of these cases.

The FWHM resolution in each of the three orthogonal directions is roughly 1 mm for source positions within the 40 mm diameter area that is of particular interest for the new scanner. Simultaneously, the sensitivity is greater than 7.3% for a point source located at the center of the scanner. Hence, these simulations indicate that the scanner will meet, and possibly exceed, the design goals for the new scanner.

B. Effect of Positron Range

The scanner performance expected with different PET isotopes was evaluated using a series of point source simulations similar to those described above. Sources with F-18, C-11, N-13, and O-15 isotopes were used. Simulations were also performed with the effect of positron range neglected. Because of the larger positron range for C-11, N-13, and O-15 compared to F-18, all of the sources were embedded in 10 mm diameter spheres for these simulations.

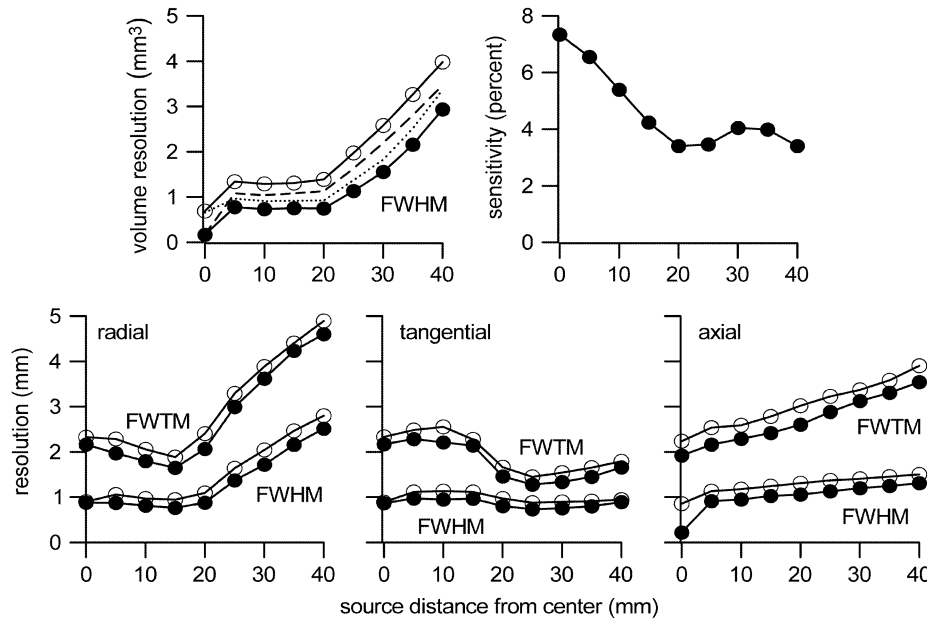


Fig. 7. Resolution and sensitivity results from F-18 point source simulations as a function of source position. The bottom row of plots shows the FWHM and FWTM resolutions in the radial, tangential, and axial directions. The upper row of plots show the FWHM volume resolution and sensitivity. Two results are given for each quantity. Open symbols indicate the results with the bank offset and midplanes options (see text) excluded. Closed symbols give the results with these options included. In addition, volume resolution results are shown for the cases in which only the bank offset (dotted line) or midplanes (dashed line) options are included. For these cases, the results in the radial, tangential, and axial directions are nearly identical to one of the two curves labeled with open or closed symbols (see text) and are not shown for the sake of clarity. The total number of coincidence events and, hence, the sensitivity, is the same for each of these cases.

The FWHM volume resolution for the five sources are shown as a function of source position in Fig. 8. Fig. 8(a) shows the results with the bank offset and midplanes options excluded in the sorting and reconstruction procedures, while Fig. 8(b) shows the results when these options are included. As expected, the resolution degrades with increasing positron range. We note that with the bank offset and midplanes options included, the FWHM volume resolution is less than 2 mm³ for each isotope within the 40 mm diameter area.

C. Hot Spot and Uniform Background Phantom

To evaluate the scanner performance using an extended source, simulations have been performed using four hot spot phantoms added to a uniform background. The background consisted of a 25 mm diameter by 30 mm long, water filled, cylindrical region. The hot spots consisted of 5 mm long cylindrical regions with diameters of 2, 3, 4, and 5 mm located in an axial plane at the center of the background cylinder. The activity concentration in each of the hot spots was chosen to be five times the concentration in the background region, and the number of decays included in the simulation was chosen to be equivalent to an imaging time of 10 min with a background concentration of 5 $\mu\text{Ci}/\text{cm}^3$. In the same manner as the point source simulations described above, images were generated for the cases with the bank offset and midplanes options included in the sorting and reconstruction procedures, and for the case with these options excluded. Sinograms were corrected for attenuation using a calculated attenuation map based on the size of the object. No scatter correction was performed. Reconstructions were performed using filtered backprojection and a Hanning filter with 100% cutoff.

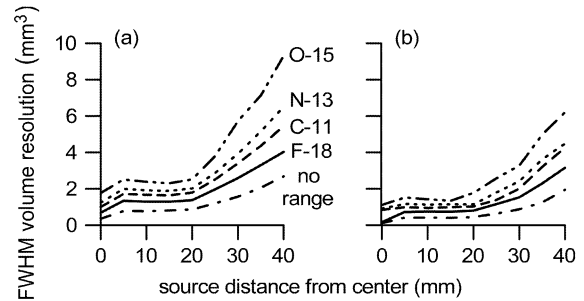


Fig. 8. Effects of position range on the volume resolution for the new scanner as determined from simulations of point sources. The FWHM volume resolution is plotted as a function of source position for F-18, C-11, N-13, and O-15 sources. Also shown are the results obtained with positron range neglected in the simulations. Plot (a) shows the results with the bank offset and midplanes options (see text) omitted. Plot (b) shows the results with these options included.

Images from the central slice of the phantom are shown in Fig. 9. Also shown in the figure are horizontal and vertical profiles through the center of the phantom. The image and profiles in the left column were obtained from the case with the bank offset and midplanes options excluded, and the right column shows the results with these options included. We observe that all of the hot spots are clearly visible in the images. As expected, partial volume effects cause the peak intensity of the smaller hot spots to be underestimated. Also, we note that the profiles are somewhat sharper for the results with the bank offset and midplanes option included. However, with these options included, the images are noisier because only half of the total imaging time is available for the two sets of the detector bank pairs used to obtain the interspersed lines of response.

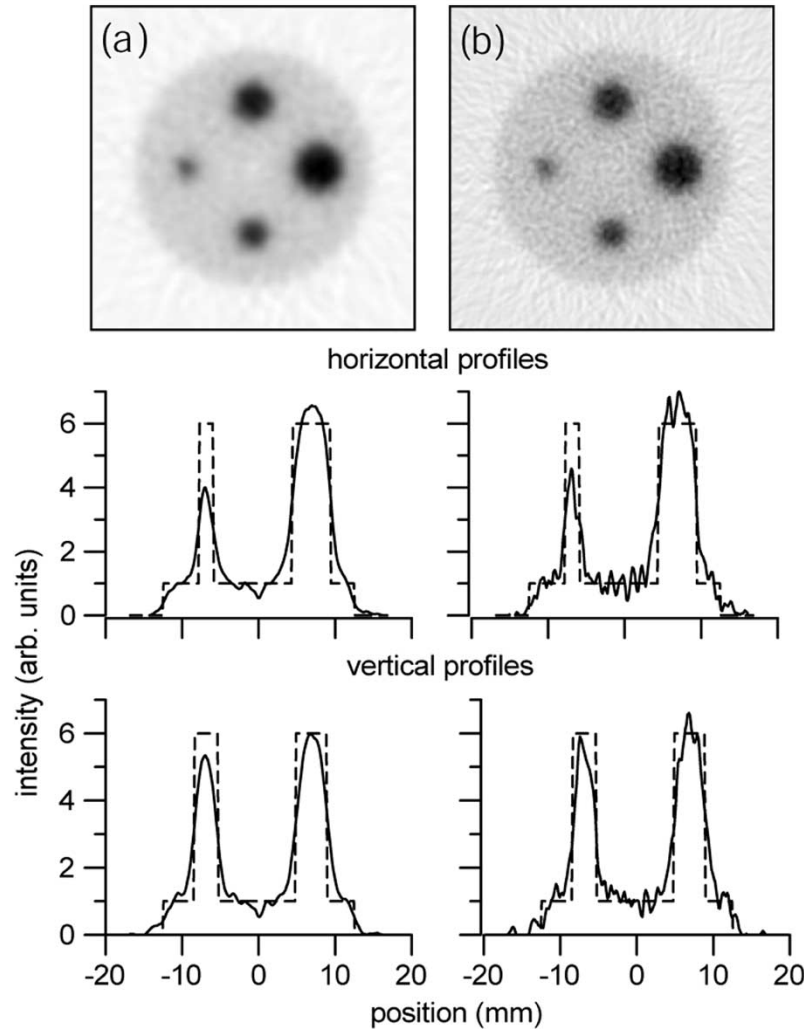


Fig. 9. Images and profiles for the hot spot phantom and background phantom. Column (a) shows the image and profiles obtained when the bank offset and midplanes options (see text) were excluded. Column (b) shows the results when these options are included. The dashed lines indicate profiles from the original phantom (not shown).

IV. DISCUSSION AND CONCLUSION

Based on the simulation results and tests presented here, we conclude that it will be possible to construct a small animal PET scanner that will achieve 1 mm FWHM resolution in the three orthogonal directions throughout a volume suitable for whole body mouse imaging and, simultaneously, a sensitivity of greater than 7% for a point source located at the center of the scanner. Also, our simulations indicate that the performance of the scanner for PET isotopes with a larger positron range compared to F-18 will not be seriously degraded, and that the performance with extended objects will be good.

The ability to achieve good resolution and good sensitivity simultaneously is a direct consequence of the use of plane detector banks. By observing coincidence events between opposing banks, parallax is minimized so that thinner crystals can be used to achieve high resolution, and at the same time, longer crystals can be used to achieve high sensitivity. Also, this configuration avoids the use of depth-of-interaction capability in the detectors.

The use of gantry rotation in the current design is critical. One benefit introduced by rotation is that, throughout a region deter-

mined by the width of the detector banks, the entire sinogram space can be completely sampled using only coincidence events between opposing detector banks. Then masking, as shown in Fig. 5, can be applied to remove lines of response that are particularly sensitive to parallax, giving a more uniform resolution throughout the FOV. A second benefit of rotation is that pairs of detector banks can be offset to give interspersed lines of response and an increase in resolution by approximately 20%. The primary difficulty introduced by gantry rotation is the increased complexity of the mechanical design and detector alignment. These issues are particularly important for the current design because of the very small array pitch used in the detectors. However, for the IndyPET [1] and IndyPET-II [2] scanners, we have developed alignment procedures that utilize gantry rotation to determine the detector positions accurately, and we do not anticipate difficulty implementing these procedures for the new design.

One difficulty introduced by the use of plane detector banks and masking is that, as shown in Fig. 7, the sensitivity decreases with distance from the center of the FOV. This effect is caused by the use of the mask shown in Fig. 5 to remove lines of response sensitive to parallax and thereby obtain a resolution

that is approximately uniform throughout a 40 mm diameter FOV suitable for whole body mouse imaging. For larger animals such as rats, the increased radial resolution and decreased sensitivity will degrade the imaging performance at larger radial positions. However, it should be easy to improve the performance for larger subjects by modeling the parallax introduced by the tilted detector banks and thereby eliminating the need for masking. Methods to compensate for this parallax by deconvolution of the point spread function for lines of response involving tilted banks, or by incorporating this effect in the system model for iterative reconstruction, are currently underway.

We emphasize that the performance results presented in this report are based on the use of the SimSET [18] package. To the best of our knowledge, this package has not been validated for a detector arrangement similar to the proposed scanner. Furthermore, as described in Section III, the only attempt to account for the intracrystal reflector in the detectors was through a simple geometrical correction factor, and no attempt was made to account for the reflector when tracking photons through the crystal arrays. It is difficult to predict in detail how these factors will affect scanner performance, so the results presented in this report must be understood as results for the specific simulations performed. Nevertheless, these results are sufficiently encouraging that development of a scanner based on the design presented in this report is continuing.

ACKNOWLEDGMENT

The authors would like to thank the reviewers for many helpful comments. This project would not be possible without extensive support from Concorde Microsystems, Inc., and CPS Innovations, Inc. In particular, we thank Robert Nutt, John Young, and Ron Nutt for valuable discussions and assistance. We also thank Michael Miller and Victor Soon of Indiana University School of Medicine, Adam Alessio of Notre Dame University, and Keith Vaigneur of Agile Engineering, Inc. for valuable discussions and technical support.

REFERENCES

- [1] T. Frese, N. C. Rouze, C. A. Bouman, K. Sauer, and G. D. Hutchins, "Quantitative comparison of FBP, EM, and Bayesian reconstruction algorithms for the IndyPET scanner," *IEEE Trans. Med. Imaging*, vol. 22, pp. 258–276, 2003.
- [2] N. C. Rouze and G. D. Hutchins, "Design and characterization of indyPET-II: A high-resolution, high-sensitivity dedicated research scanner," *IEEE Trans. Nucl. Sci.*, vol. 50, pp. 1491–1497, 2003.

- [3] C. J. Marriott, J. E. Cadorette, R. Lecomte, V. Scasnar, J. Rousseau, and J. E. van Lier, "High-resolution PET imaging and quantitation of pharmaceutical biodistributions in a small animal using avalanche photodiode detectors," *J. Nucl. Med.*, vol. 35, pp. 1390–1396, 1994.
- [4] P. M. Bloomfield, R. Myers, S. P. Hume, T. J. Spinks, A. A. Lammertsma, and T. Jones, "Three-dimensional performance of a small-diameter positron emission tomograph," *Phys. Med. Biol.*, vol. 42, pp. 389–400, 1997.
- [5] S. R. Cherry, Y. Shao, R. W. Silverman, K. Meadors, S. Siegel, A. Chatzioannou, J. W. Young, W. Jones, J. C. Moyers, D. Newport, A. Boufennouchet, T. H. Farquhar, M. Andreaco, M. J. Paulus, D. M. Binkley, R. Nutt, and M. E. Phelps, "MicroPET: A high resolution PET scanner for imaging small animals," *IEEE Trans. Nucl. Sci.*, vol. 44, pp. 1161–1166, 1997.
- [6] M. Watanabe, H. Okada, K. Shimizu, T. Omura, E. Yoshikawa, T. Koguchi, S. Mori, and T. Yamashita, "A high resolution animal PET scanner using compact PS-PMT detectors," *IEEE Trans. Nucl. Sci.*, vol. 44, pp. 1277–1282, 1997.
- [7] S. Weber, A. Terstegge, H. Herzog, R. Reinartz, P. Reinhart, F. Rongen, H. W. Muller-Garmer, and H. Halling, "The design of an animal PET: Flexible geometry for achieving optimal spatial resolution or high sensitivity," *IEEE Trans. Med. Imaging*, vol. 16, pp. 684–689, 1997.
- [8] A. Del Guerra, G. Domenico, M. Scandola, and G. Zavattini, "YAP-PET: First results of a small animal positron emission tomograph based on YAP:Ce finger crystals," *IEEE Trans. Nucl. Sci.*, vol. 45, pp. 3105–3108, 1998.
- [9] J. A. Correia, C. A. Burnham, D. Kaufman, and A. J. Fischman, "Development of a small animal PET imaging device with resolution approaching 1 mm," *IEEE Trans. Nucl. Sci.*, vol. 46, pp. 631–635, 1999.
- [10] J. S. Huber and W. W. Moses, "Conceptual design of a high-sensitivity small animal PET camera with 4π coverage," *IEEE Trans. Nucl. Sci.*, vol. 46, pp. 498–502, 1999.
- [11] A. P. Jeavons, R. A. Chandler, and C. A. R. Dettmar, "A 3D HIDAC-PET camera with sub-millimeter resolution for imaging small animals," *IEEE Trans. Nucl. Sci.*, vol. 46, pp. 468–473, 1999.
- [12] R. S. Miyaoka, S. G. Kohlmyer, and T. K. Lewellen, "Performance characteristics of micro crystal element (MiCE) detectors," *IEEE Trans. Nucl. Sci.*, vol. 48, pp. 1403–1407, 2001.
- [13] Y. C. Tai, A. Chatzioannou, S. Siegel, J. Young, D. Newport, R. N. Goble, R. E. Nutt, and S. R. Cherry, "Performance evaluation of the microPET P4: A PET system dedicated to animal imaging," *Phys. Med. Biol.*, vol. 46, pp. 1845–1862, 2001.
- [14] S. I. Ziegler, B. J. Pichler, G. Boening, M. Rafecas, W. Pimpl, E. Lorenz, N. Schmitz, and M. Schwaiger, "A prototype high-resolution animal positron tomograph with avalanche photodiode arrays and LSO crystals," *Eur. J. Nucl. Med.*, vol. 28, pp. 136–143, 2001.
- [15] J. Seidel, J. J. Vaquero, and M. V. Green, "Resolution uniformity and sensitivity of the NIH ATLAS small animal PET scanner: Comparison to simulated LSO scanners without depth-of-interaction capability," *IEEE Trans. Nucl. Sci.*, vol. 50, pp. 1347–1350, 2003.
- [16] C. Knoess, S. Siegel, A. Smith, D. Newport, N. Richerzhagen, A. Winkler, A. Jacobs, R. Goble, R. Graf, K. Wienhard, and W. Heiss, "Performance evaluation of the microPET R4 PET scanner for rodents," *Eur. J. Nucl. Med. Mol. Imaging*, vol. 30, pp. 737–747, 2003.
- [17] Y. C. Tai, A. F. Chatzioannou, Y. Yang, R. W. Silverman, K. Meadors, S. Siegel, D. F. Newport, J. R. Stickel, and S. R. Cherry, "MicroPET II: Design, development, and initial performance of an improved microPET scanner for small-animal imaging," *Phys. Med. Biol.*, vol. 48, pp. 1519–1537, 2003.
- [18] T. K. Lewellen, R. L. Harrison, and S. Vannoy, "The SimSET program," in *Monte Carlo Calculations in Nuclear Medicine*, M. Ljungberg, S. E. Strand, and M. A. King, Eds. Bristol, MA: IOP, 1998, pp. 77–92.
- [19] M. Defrise, P. E. Kinahan, D. W. Townsend, C. Michel, M. Sibomana, and D. F. Newport, "Exact and approximate rebinning algorithms for 3-D PET data," *IEEE Trans. Med. Imaging*, vol. 16, pp. 145–158, 1997.